Eur. Phys. J. E (2020) **43**: 5
DOI 10.1140/epje/i2020-11930-7

THE EUROPEAN PHYSICAL JOURNAL E

Regular Article

Simultaneous melting and solidification of a columnar dendritic microstructure in a temperature gradient: Numerical modeling and experiments***

Chongchen Xiang[1], Qingyu Zhang[1,a], Dongke Sun[2], Shunhu Zhang[1], Mingfang Zhu[3], and Markus Rettenmayr[4]

[1] Shagang School of Iron and Steel, Soochow University, Suzhou 215137, China
[2] School of Mechanical Engineering, Southeast University, Nanjing 211189, China
[3] Jiangsu Key Laboratory of Advanced Metallic Materials, School of Materials Science and Engineering, Southeast University, Nanjing 211189, China
[4] Otto Schott Institute of Materials Research, Friedrich-Schiller-Universität, Löbdergraben 32, Jena 07743, Germany

Received 25 June 2019 and Received in final form 2 December 2019
Published online: 30 January 2020
© EDP Sciences / Società Italiana di Fisica / Springer-Verlag GmbH Germany, part of Springer Nature, 2020

Abstract. The microstructural evolution of a SCN-ACE alloy in a temperature gradient is studied by cellular automaton (CA) modeling and *in situ* experiments. The initially columnar dendrites gradually evolve to a completely solid region with a planar solid/liquid interface. The CA simulations and *in situ* observations present the migration of secondary dendrite arms and liquid pockets due to temperature gradient zone melting (TGZM), and the movement of the interface between a mushy zone and a fully liquid zone. The CA simulations show that the interface movement toward the lower temperature region is caused by the increasing concentration of the fully liquid region. Through updating the concentration in the fully liquid zone to the initial concentration in the CA simulation for mimicking the efficient stirring in liquid, the movement of the interface between the mushy zone and the fully liquid zone is hindered. The simulated liquid fractions and mean concentrations throughout the mushy zone decrease with time, which agree well with the analytical predictions. The simulated concentrations in the resolidified mushy zone are not higher than the temperature-dependent solidus concentrations, implying that no supersaturation remains after the mushy zone fully solidifies.

1 Introduction

When the mushy zone of an alloy is situated in a temperature gradient, simultaneous melting and solidification processes lead to a series of complex phenomena, *e.g.*, liquid film migration (LFM) and dendrite coarsening [1]. These processes influence the microstructure and concentration distribution in the mushy zone of an alloy significantly, and hence receive much attention in the fields of production of thermoelectric materials [2], synthesis of pure intermetallic phases [3], measurement of thermophysical property [4,5], and crystal growth [6]. During holding in a temperature gradient, the local liquid concentrations in the mushy zone can be assumed to approximately follow the temperature-dependent local liquidus concentrations [7, 8]. As a result, a macroscopic concentration gradient is generated in the liquid throughout the mushy zone, giving rise to solute transport toward higher temperatures [8–10]. The solute transport is accompanied by simultaneous melting and solidification processes in the mushy zone, and the interaction between these physical processes is a prominent research topic in academia [11–17]. In particular, the local melting and solidification lead to either liquid pockets or secondary dendrite arms in the mushy zone moving towards higher temperature, and this phenomenon is termed temperature gradient zone melting (TGZM) [1, 18]. The mechanism of TGZM can be found elsewhere for detail [18], and the essence is briefly described here. For a liquid pocket in the mushy zone during temperature gradient holding, local solute enrichment and depletion occur at the hotter and colder solid/liquid (S/L) interfaces, respectively, driven by the directional solute transport.

* Contribution to the Topical Issue "Branching Dynamics at the Mesoscopic Scale" edited by Yongsheng Han, Hui Xing, Dongke Sun.

** Supplementary material in the form of two .mpg file(s) available from the Journal web page at
https://doi.org/10.1140/epje/i2020-11930-7

[a] e-mail: qingyu.zhang@suda.edu.cn
(corresponding author)

The solute enrichment causes local melting of the hotter solid/liquid interface of the liquid pocket, while the solute depletion leads to local solidification of the colder solid/liquid interface. As a result, the liquid pockets show the moving behavior toward the high-temperature direction. Since liquid pockets locate in the middle of neighboring secondary dendrite arms, the TGZM effect described above for liquid pockets is equivalent to that a sequence of secondary dendrite arms migrate towards the high-temperature direction.

Salloum-Abou-Jaoude *et al.* [14] carried out *in situ* experiments observing the mushy zone evolution of an Al-Cu alloy in a static temperature gradient by means of synchrotron X-ray radiography. In the *in situ* experiments, the evolution of the concentration distribution in the liquid and of the dendritic microstructure is characterized. However, due to the difficulties of quantitatively measuring solute concentrations in the solid and liquid phases in real time, the behavior of melting/solidification and solute transport for an initially dendritic microstructure in a temperature gradient has not yet been characterized exhaustively in experimental studies.

Theoretical models were developed to describe the melting/solidification processes and mushy zone dynamics in a temperature gradient [7,19]. A one-dimensional (1-D) analytical model was proposed by Combeau-Appolaire-Seiler (CAS) [7] to predict the evolution of liquid fraction and local mean concentration in the mushy zone. In this model, the assumption of instantaneous thermodynamic equilibration at the solid/liquid interfaces was adopted, and the results are continuous functions of the position in the mushy zone. The CAS model predicts that the mushy zone with a constant length completely solidifies in the final stage, and the final mean concentrations are equal to the temperature-dependent local solidus concentration. Pan *et al.* [19] proposed a 1-D analytical model to describe the migration of liquid regions due to TGZM, providing the location and migration velocity of a moving liquid region in the mushy zone. However, this model is not designed to predict the evolution of quantities such as liquid fraction and local mean concentration along the mushy zone. Overall, the above analytical models both neglect the curvature effect, and thus are unable to reproduce the evolution of a dendritic microstructure in the mushy zone during holding in a temperature gradient.

In addition to the experimental observations and theoretical analyses, numerical modeling provides an alternative tool to study the microstructural evolution during alloy solidification [20–27]. Regarding the study of mushy zone dynamics in a temperature gradient, Boussinot and Apel [28] performed phase-field simulations of the microstructural evolution from an initially dendritic morphology to a planar S/L interface. The simulation results indicate that the interface between mushy zone and fully liquid zone moves towards lower temperatures, and the mushy zone becomes shorter than the predicted by calculations using equilibrium phase diagram data (liquidus and solidus temperatures) and the temperature gradient. Some of the present authors applied a cellular automaton (CA) model involving both solidification and melting to simulate the microstructural evolution of columnar dendrites and equiaxed grains in a temperature gradient [29]. The migration of the secondary dendrite arms and liquid pockets in the mushy zone due to TGZM was visualized. The simulated holding time in the CA calculations was too short to reach the final planar S/L interface.

In the present study, a recently proposed CA model that includes both solidification and melting [29,30] is applied to simulate the microstructural evolution of columnar dendrites of a SCN-ACE alloy during holding in a temperature gradient. A comparison of the simulated microstructures and *in situ* experimental observations is presented. As compared to the previous work of the present authors [18], the computation domain in the present study is large enough to cover the entire mushy zone, and the physical time for the CA simulation of temperature gradient holding is much longer. The microstructural evolution from columnar dendrites to a planar interface during resolidification of the mushy zone is analyzed in detail. The movement mechanism of the interface between the mushy zone and the fully liquid zone is investigated by the CA simulations. The simulated evolution of the liquid fraction and concentration distribution throughout the mushy zone is compared with analytical predictions.

2 Cellular automaton model and in situ experimental observation

The CA model has the capability to quantitatively simulate melting and solidification of alloys simultaneously, which has been validated in the previous articles [18,30]. According to the local composition equilibrium approach in the CA model, during a given time step, the increment of the solid fraction in an interface cell is calculated by

$$\Delta f_s = g \cdot \frac{(C_l^{eq} - C_l^*)}{C_l^{eq}(1-k)}\,, \tag{1}$$

where g is a geometrical factor for reducing the artificial anisotropy (the detailed algorithm for calculating g can be found elsewhere [18,30]); k (= 0.1) is the partition coefficient for SCN-ACE; C_l^{eq} and C_l^* are the local equilibrium liquid concentration and local actual liquid concentration, respectively. Equation (1) denotes that the kinetics of solidification and melting is determined by the difference between C_l^{eq} and C_l^*. C_l^{eq} is calculated by

$$C_l^{eq} = \frac{T^* - T_m}{m_l} + \frac{\Gamma \overline{K} f(\varphi, \theta_0)}{m_l}\,, \tag{2}$$

where T^* is the local interface temperature, T_m (= 58.081 °C) is the melting point of pure SCN, m_l (= −2.8 °C/wt.%) is the slope of the liquidus in the SCN-ACE phase diagram. Γ (= 6.48×10^{-8} °C · m) is the Gibbs-Tomson coefficient, $\overline{K}$ is the local curvature evaluated from the solid fraction gradient at the S/L interface, and $f(\varphi, \theta_0)$ is a function accounting for the anisotropy of the interfacial energy. Apparently, the first term on the right-hand side of eq. (2) is the temperature-dependent

liquidus concentration, and the second term represents the contribution of the curvature undercooling. C_l^* is determined by solving the diffusion equation

$$\frac{\partial C}{\partial t} = \nabla \cdot (D(f_s)\nabla(C/p(f_s))), \tag{3}$$

where $C = C_s f_s + C_l(1 - f_s)$ is the mean concentration, $D(f_s)$ is the diffusion coefficient evaluated by $D(f_s) = kD_s f_s + D_l(1 - f_s)$, where D_s ($= 3 \times 10^{-13}\,\mathrm{m}^2/\mathrm{s}$) and D_l ($= 3 \times 10^{-9}\,\mathrm{m}^2/\mathrm{s}$) are the diffusivities of solute ACE in the solid and liquid phases, respectively. The conversion coefficient function, $p(f_s)$, is calculated by $p(f_s) = kf_s + (1 - f_s)$. A zero-flux boundary condition is adopted on all walls of the two-dimensional domain. In the CA model, the evolution time and the spatial length are both physical.

In addition to the CA simulation, *in situ* experimental observations of the microstructural evolution in the mushy zone of a transparent organic SCN-ACE alloy were carried out using a Bridgman-type solidification set-up. The experimental set-up is described in detail elsewhere [18]. In the *in situ* experiments, the microstructural evolution of the columnar dendrites occurred in a rectangular glass tube with a thin cavity ($\sim 200\,\mu$m). The rectangular glass tube was placed horizontally and kept stationary. In the process of temperature gradient holding, the convective flows caused by the buoyancy effect and glass tube movement can be neglected. The experiments were performed in two stages. In the first stage, directional solidification of a SCN-1.5 wt%ACE alloy was conducted to obtain columnar dendrites, under the conditions of a temperature gradient of $G = 4.5\,^\circ$C/mm and a pulling velocity of $V_p = 17.7\,\mu$m/s. The pulling of the sample was stopped when the columnar dendrites were growing in a steady state, and the columnar dendrites were held in the temperature gradient. The microstructural evolution was observed and recorded by an optical microscope equipped with a CCD camera.

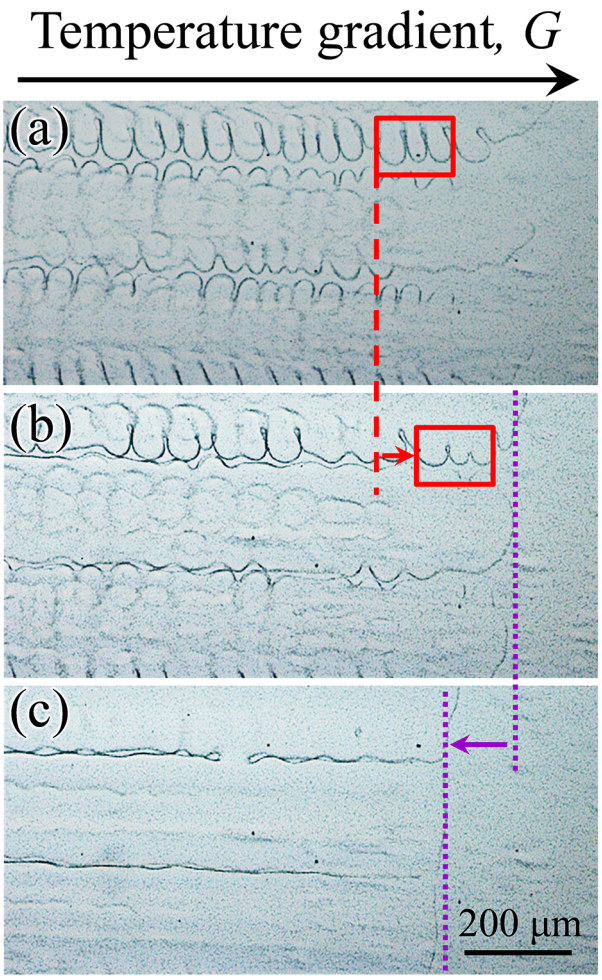

Fig. 1. *In situ* experimental observation of microstructural evolution of columnar dendrites of a SCN-1.5 wt%ACE alloy in a temperature gradient of $G = 4.5\,^\circ$C/mm. The photos were taken at (a) $t = 20$ s, (b) $t = 134$ s, and (c) $t = 320$ s after stopping pulling the sample.

3 Results and discussion

3.1 Microstructural evolution from columnar dendrites to a planar S/L interface

In situ experiments and CA simulations including both local melting and local solidification are performed for a SCN-1.5 wt%ACE alloy to study the microstructural evolution in the mushy zone. Figure 1 exhibits experimental micrographs of the microstructures of the SCN-1.5 wt%ACE alloy during holding in a temperature gradient of $G = 4.5\,^\circ$C/mm, taken at 20 s, 134 s, and 320 s after stopping pulling the sample. The micrographs in fig. 1 are processed digitally in order to better display the microstructural features. Due to the limitation in the field of view of the optical microscope, fig. 1 only covers a portion of the mushy zone. As shown in fig. 1(a), after a 20 s holding period, the side branches of the columnar dendrite still can be identified clearly. After 134 s (fig. 1(b)), however, the profiles of the secondary dendrite arms become obscure. As marked by the red boxes in fig. 1(a) and (b), it can be seen that the side arms migrate towards higher temperatures. The migration of the side arms is due to TGZM, which has been discussed in detail elsewhere [18]. In fig. 1(c), it is observed that the secondary dendrite arms cannot be distinguished any more, and long liquid channels between the former primary trunks have formed. Moreover, fig. 1 shows that the tip region of the former primary trunks gradually evolves to a nearly planar interface. As indicated by the dotted lines in fig. 1(b) and (c), the interface between the mushy zone and the bulk liquid region moved towards lower temperatures. As a result, the fully liquid region expands, while the length of the mushy zone shrinks during holding in the temperature gradient.

The CA model is applied to study the mushy zone dynamics of a SCN-1.5 wt%ACE alloy in a temperature gradient of $G = 10\,^\circ$C/mm. The somewhat higher gradient was chosen to limit the calculation time until the mushy zone is fully solidified. The initial dendritic microstructure and concentration field are generated by simulating

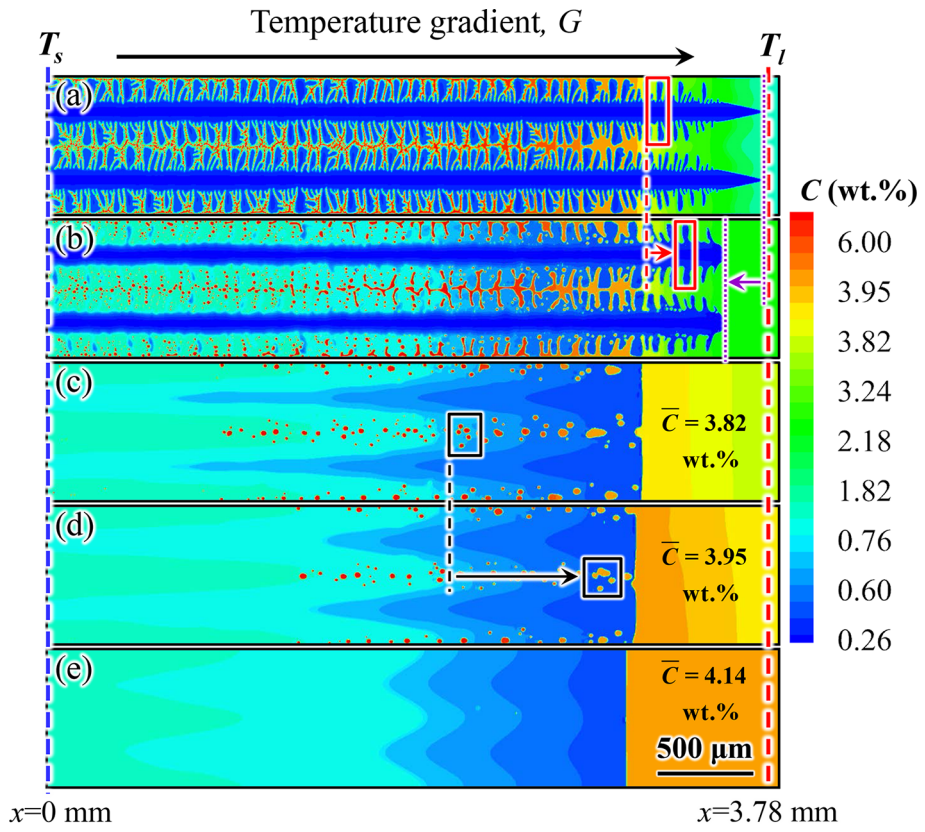

Fig. 2. Simulated evolution of columnar dendrites (shown by the concentration field) of a SCN-1.5 wt%ACE alloy in a temperature gradient of $G = 10\,^{\circ}\mathrm{C/mm}$: (a) $t = 0\,\mathrm{s}$; (b) $t = 120\,\mathrm{s}$; (c) $t = 3000\,\mathrm{s}$; (d) $t = 4000\,\mathrm{s}$; (e) $t = 7650\,\mathrm{s}$. $\overline{C}$ in panels (c)–(e) is the mean concentration of the bulk liquid region. The red and black boxes mark the secondary dendrite arms and liquid pockets at different times, respectively. The evolution of the columnar dendrites can also be seen in the supplementary video 1.

directional solidification of the SCN-1.5 wt%ACE alloy in a temperature gradient of $G = 10\,^{\circ}\mathrm{C/mm}$ and a pulling velocity of $V_p = 50\,\mu\mathrm{m/s}$. Then, the pulling velocity is assigned as $V_p = 0$, and thus the columnar dendrites are held in the static temperature gradient. In the CA simulation, the computation domain consists of a 1310×240 mesh with a mesh size of $\Delta x = 3\,\mu\mathrm{m}$. Figure 2 presents the simulated microstructural evolution in the mushy zone (shown in the concentration field) during holding in the temperature gradient (see also the supplementary video 1). It can be seen that the initially dendritic microstructure gradually transforms into a solid region with a planar interface towards the fully liquid region. As shown in fig. 2(a), the position of the solidus temperature ($T_s = 16.08\,^{\circ}\mathrm{C}$) is at $x = 0\,\mathrm{mm}$, while the liquidus temperature ($T_l = 53.88\,^{\circ}\mathrm{C}$) of the initial composition is at $x = 3.78\,\mathrm{mm}$, which is close to the position of the tips of the columnar dendrites. After a 120 s holding period (fig. 2(b)), in the low temperature region the primary trunks of the former columnar dendrites can still be identified, whereas the outlines of the former side arms become invisible. Moreover, small solute enriched liquid pockets have formed in the space between the former dendrite arms. In the high-temperature region, it can be seen that the dendrite arms become coarser. As indicated by the red boxes in fig. 2(a) and (b), the secondary dendrite arms migrate towards higher temperatures due to TGZM, which is identical to the experimental observation in fig. 1 and our previous study [18]. On the other hand, as shown by the dotted lines in fig. 2(a) and (b), the tips of the primary dendrites remelt, and the S/L interfaces of the primary dendrite tips move towards lower temperatures. In fig. 2, it can be seen how the columnar dendrites gradually evolve to a fully solidified zone with a planar S/L interface, which agrees well with the experimental observation in fig. 1. As marked by the black boxes in fig. 2(c) and (d), the liquid pockets in the solid matrix migrate towards the high-temperature direction due to TGZM, and finally enter the fully liquid zone. During the migration of the liquid pockets, they may coalesce with neighboring ones, and their shapes and concentrations change with time. In fig. 2(e), no liquid pockets remain in the solid zone. Evidently, due to solute partitioning at the S/L interface the concentrations of the liquid pockets are higher than those of the solid phase. Thus, the migration of the solute enriched liquid pockets due to TGZM transports the solute towards higher temperatures. This contributes to an increase of the mean concentration in the bulk liquid region ($\overline{C}$ in fig. 2(c)–(e)) with time. Apparently, solute enrichment is formed in the bulk liquid zone. In addition, it can be seen in fig. 2 that the mushy zone/bulk liquid region interface moves towards lower temperatures, leading to a gradually shorter mushy zone.

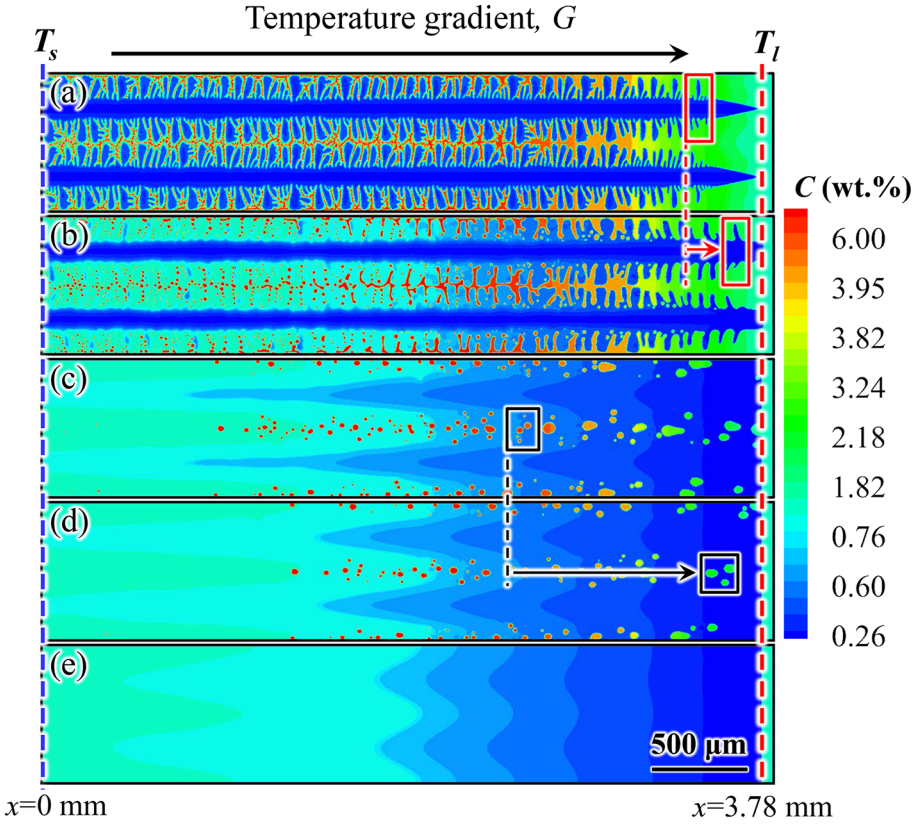

Fig. 3. Simulated evolution of columnar dendrites (shown by the concentration field) of a SCN-1.5 wt%ACE alloy in a temperature gradient of $G = 10\,^{\circ}\mathrm{C/mm}$ with resetting the concentrations in the fully liquid zone to the initial concentration at each time step: (a) $t = 0\,\mathrm{s}$; (b) $t = 120\,\mathrm{s}$; (c) $t = 3000\,\mathrm{s}$; (d) $t = 4000\,\mathrm{s}$; (e) $t = 7650\,\mathrm{s}$. The red and black boxes mark the secondary dendrite arms and liquid pockets at different times, respectively. The evolution of the columnar dendrites can also be seen in the supplementary video 2.

In order to investigate the effect of solute enrichment on the movement of the mushy zone/bulk liquid region interface, the CA simulation was carried out with resetting the concentrations in the fully liquid zone to the initial concentration (C_0 = 1.5 wt% ACE) at each time step. This could be considered to mimic the efficient stirring in the fully liquid zone, *e.g.* the experimental studies where long samples are heated by induction that causes forced convection [9]. The other simulation conditions are the same as those of fig. 2. Figure 3 displays the evolution of the concentration field of the initially dendritic microstructure during holding in the temperature gradient (see also the supplementary video 2). Similar to the case of fig. 2, the mushy zone gradually solidifies, and the migration of the secondary dendrite arms and of solute enriched liquid pockets due to TGZM are also observed in fig. 3. However, with increasing holding time, the interface between the mushy zone and the fully liquid region remains at the position of the liquidus temperature. Figure 3 indicates that the movement of the interface between the mushy zone and the fully liquid zone is hindered by eliminating the solute enrichment in the bulk liquid region.

3.2 Evolution of liquid fraction and concentration distribution in the mushy zone

In addition to the microstructural evolution shown in figs. 2 and 3, the simulated liquid fraction and local mean concentrations in the mushy zone at different holding times are plotted and compared to the CAS model predictions. According to the CAS model, the liquid fraction, f_l, can be calculated by [7]

$$\frac{\partial f_l}{\partial t} = -D_l \frac{G}{(T_l - T_s)[1-(1-k)x/l_T]} \frac{\partial f_l}{\partial x}\,, \qquad (4)$$

where t and x are the holding time and the 1-D position in the mushy zone, respectively; l_T is the mushy zone length calculated according to the liquidus and solidus temperatures, and the temperature gradient, which is $l_T = (T_l - T_s)/G = 3.78\,\mathrm{mm}$ in the present study. Figure 4 presents the comparison of liquid fractions varying with the position in the mushy zone (and thus temperature) after different holding times, obtained from the CA simulations and the CAS model. The symbols and lines represent

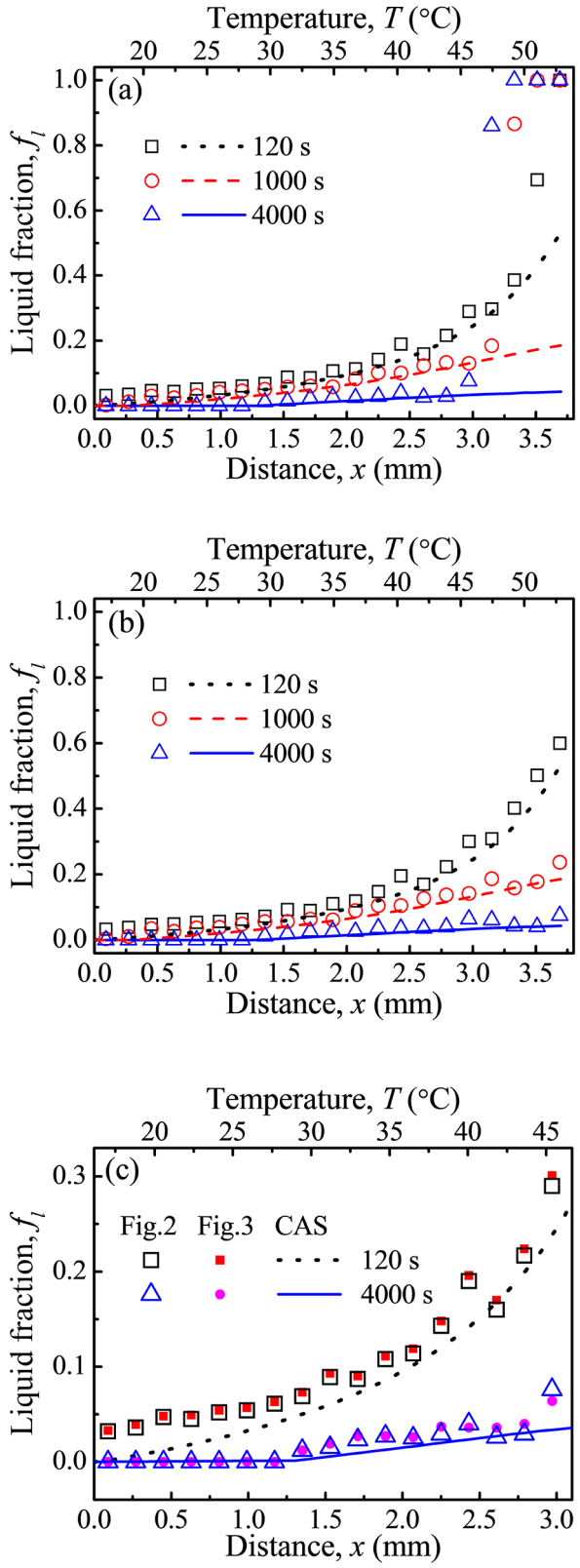

Fig. 4. Comparison of local liquid fractions at different holding times between the CA simulations (symbols) and the CAS model predictions (lines) [7]: (a) CA simulation in fig. 2; (b) CA simulation in fig. 3; (c) data in the mushy zone of $x \leq 3.0\,\text{mm}$ in figs. 2 and 3.

the CA simulation results and the CAS model predictions, respectively. The simulation results are obtained by averaging the data over the rectangular regions ($180 \times 720\,\mu\text{m}$) along the mushy zone. The simulated data in fig. 4(a) and (b) correspond to the CA simulations without and with resetting all concentrations in the fully liquid region to the initial concentration (figs. 2 and 3), respectively. As shown in fig. 4, the simulated liquid fractions are subject to fluctuations. The reason is that the liquid pockets exhibit non-uniform spatial distribution throughout the mushy zone, as seen in figs. 2 and 3. For each holding time, the simulated data and the CAS model predictions show how the liquid fractions increase with increasing mushy zone temperature. As indicated in fig. 4(a), the liquid fractions at different positions of the mushy zone decrease with time, but the simulated liquid fractions in the expanding fully liquid region are equal to unity. Nevertheless, it is considered that the simulated data agree well with the solution of the CAS model in the regions that are not included in the fully liquid region. In fig. 4(b), the influence of the expanding fully liquid region is excluded. It is seen that in the high-temperature region the liquid fractions are still in good agreement with the CAS model. Figure 4(c) presents the comparison of the liquid fractions in the mushy zone of $x \leq 3.0\,\text{mm}$, where x is the distance from the solidus, obtained from the CA simulations of figs. 2 and 3 and the CAS model, at the holding times of 120 s and 4000 s, respectively. It is found that the simulated liquid fractions have negligible differences in the cases with and without updating the concentrations in the fully liquid region.

Figure 5 shows a comparison of the local mean concentrations varying with mushy zone position (and temperature) after different holding times, obtained from the CA simulations and the CAS model. At each temperature, the CAS model prediction of the mean concentration is obtained by $\bar{C}(T) = C^{eq}_{Sol}(T) \cdot [1 - f_l(T)] + C^{eq}_{Liq}(T) \cdot f_l(T)$, where $C^{eq}_{Sol}(T)$ and $C^{eq}_{Liq}(T)$ are temperature-dependent solidus and liquidus concentrations, respectively. Similar to fig. 4, the simulated data display fluctuations, while the CAS model predictions are continuous functions. It is seen in fig. 5 that the simulated local mean concentrations at different mushy zone positions decrease with time. In fig. 5(a), however, the simulated local mean concentrations in the fully liquid region are found to increase with time. The decrease of the mean concentrations in the solid quantifies the solute transport out of the mushy zone, while the increase of the simulated local mean concentrations in fig. 5(a) in the high-temperature region shows that the solute is incorporated in the fully liquid zone and thus causes solute enrichment. In fig. 5(b), the solute transport out of the mushy zone without solute enrichment in the fully liquid region is shown. Figure 5(c) presents the comparison of the local mean concentrations in the mushy zone of $x \leq 3.0\,\text{mm}$ obtained from figs. 2 and 3 and the CAS model, at the holding times of 120 s and 4000 s, respectively. Similar to fig. 4(c), the local mean concentrations have negligible differences in the CA simulations with and without updating concentrations in the fully liquid region.

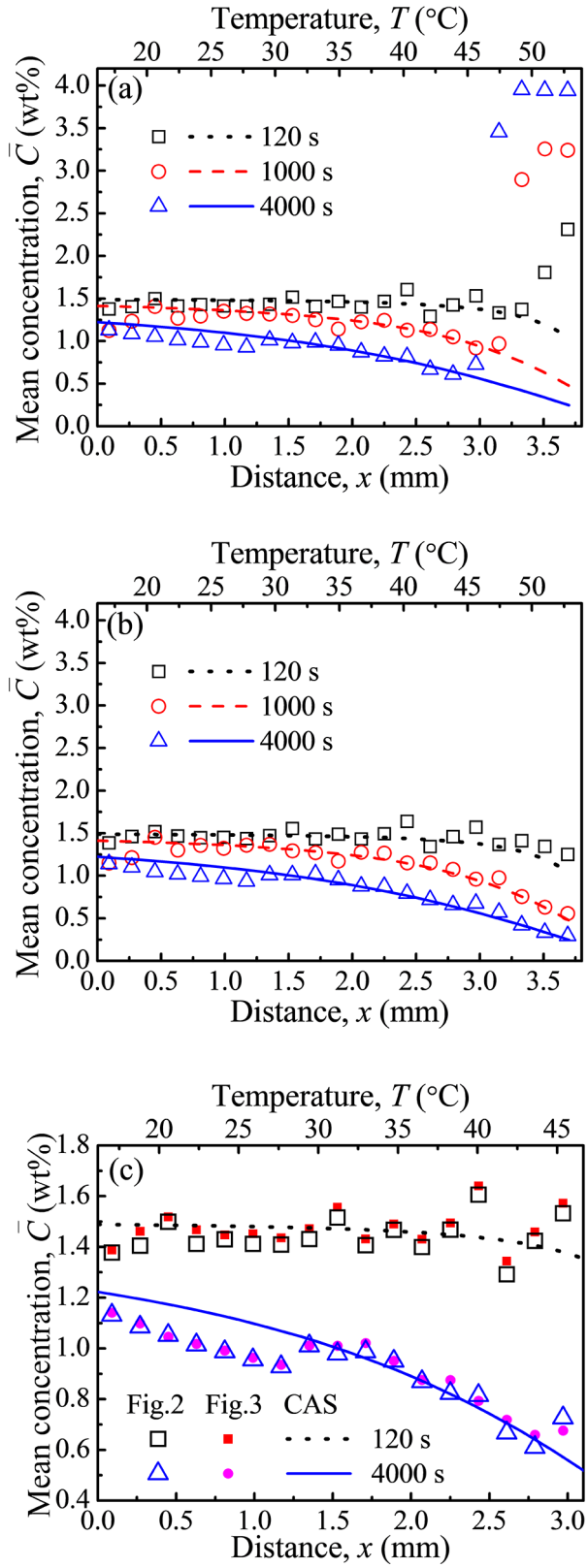

Fig. 5. Comparison of local mean concentrations after different holding times between the CA simulations (symbols) and the CAS model predictions (lines) [7]: (a) CA simulation in fig. 2; (b) CA simulation in fig. 3; (c) data in the mushy zone of $x \leq 3.0$ mm in figs. 2 and 3.

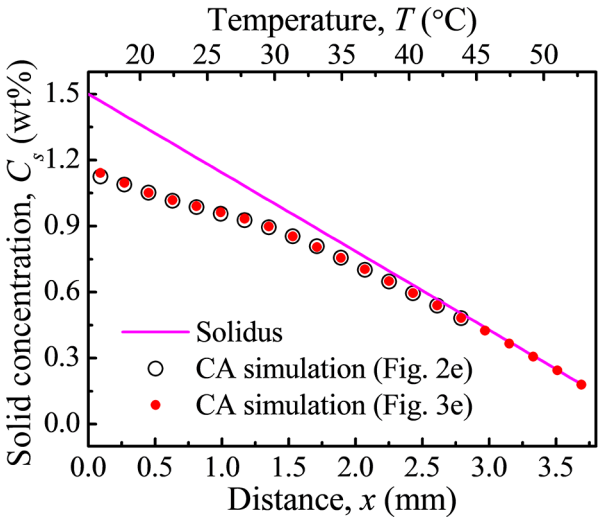

Fig. 6. Comparison of the simulated solid concentrations along the solidified mushy zone obtained from the CA simulations corresponding to figs. 2(e) and 3(e), respectively. The solidus line is also plotted.

In order to study the effect of mimicked stirring on the concentration of the solid phase after the mushy zone has completely solidified, fig. 6 presents the comparison between the simulated solid concentration distribution and the solidus line. As shown, the solid concentrations at different positions in figs. 2(e) and 3(e) are almost superimposed, indicating that the effect of mimicked liquid stirring on the solid concentrations is negligible. In the low-temperature region, the solid concentrations are lower than the solidus concentrations. The solid concentrations gradually approach to the solidus line as the temperature increases. The simulated solid concentrations show that there is no supersaturation remaining after the mushy zone has fully solidified. Since a concentration gradient is produced in the solid phase, solid diffusion will occur until the solid phase finally reaches a stationary state with a homogeneous concentration. However, since the solid diffusivity is three orders of magnitude smaller than the liquid diffusivity, it is expected that the holding time for reaching the final stationary state will not be reached employing the currently available computing power.

In the present work, the CA simulations are performed in two dimensions. It is expected that the quantitative data obtained from the three-dimensional simulations should be closer to reality. Due to the differences of local melting/solidification kinetics and diffusion spaces, there might be some deviations of the liquid fraction and solute concentration distributions in the two- and three-dimensional cases, which still require future study.

4 Conclusions

The microstructural evolution of an initially columnar dendritic structure of a SCN-ACE alloy due to simultaneous melting and solidification in a temperature gradient is studied by CA simulations and *in situ* experimental

observation. The simulation results show that the mushy zone gradually evolves to a fully solid region with a planar S/L interface, which compares well with the *in situ* experimental observation. During holding in the temperature gradient, the migration of secondary dendrite arms and liquid pockets toward higher temperatures due to TGZM are exhibited in the CA simulations and *in situ* experimental observation. The CA simulations also reproduce the coalescence and morphological changes of the solute enriched liquid pockets, which enter the fully liquid region, and hence contribute to the increase of the concentration of the fully liquid region. The CA simulation and *in situ* experimental observation reveal how the interface between the mushy zone and the fully liquid region moves towards lower temperatures, and the mushy zone length decreases with time. This is caused by solute enrichment in the fully liquid zone. The CA simulation with resetting all concentrations in the fully liquid zone to the initial concentration indicates that the movement of the interface between the mushy zone and the fully liquid zone can be hindered by eliminating the solute enrichment in the bulk liquid region.

The CA simulated distributions of the local liquid fraction and local mean concentration in the mushy zone are analyzed and compared to CAS model predictions. With increasing holding time, the liquid fractions and mean concentrations at different positions decrease with time. The decrease of the mean concentrations is due to the solute transport out of the mushy zone. After the mushy zone has completely solidified, the mean solid concentrations at different positions are not higher than the temperature-dependent solidus concentrations, denoting that there is no supersaturation remaining in the solid matrix. The CA simulations reveal that mimicked stirring has little influence on the phase fractions and mean concentrations in the mushy zone. The simulated evolution of the local liquid fraction and local mean concentration distribution agrees well with the CAS model predictions.

This work was supported by the National Natural Science Foundation of China (Grant No. 51901148) and the Fundamental Research Funds for the Central Universities (Grant No. 2242019K1G003). CCX acknowledges the financial support from the Basic Research Program of Jiangsu Province (CN) (Grant No. BK20190831).

Author contribution statement

Chongchen Xiang and Qingyu Zhang performed the simulations and wrote the manuscript. Qingyu Zhang carried out the *in situ* experiments. Dongke Sun and Shunhu Zhang gave advices on the writing of the manuscript. Mingfang Zhu and Markus Rettenmayr revised the manuscript and helped putting the research in the scientific context.

Publisher's Note The EPJ Publishers remain neutral with regard to jurisdictional claims in published maps and institutional affiliations.

References

1. M. Rettenmayr, Int. Mater. Rev. **54**, 1 (2009).
2. H. Wang, S. Li, X. Li, H. Zhong, J. Cryst. Growth **466**, 56 (2017).
3. S. Lippmann, R.H. Kemsies, M. Schick, B. Milkereit, O. Kessler, M. Rettenmayr, K. Hack, Intermetallics **105**, 107 (2019).
4. X. Ma, T. Yoshikawa, K. Morita, Sci. Adv. Mater. **6**, 1697 (2014).
5. S. Kawanishi, T. Yoshikawa, Mater. Trans. **58**, 450 (2017).
6. J.Y. Li, L. Wang, P. Ni, Y. Tan, Mater. Sci. Semicond. Process. **66**, 170 (2017).
7. H. Combeau, B. Appolaire, J. Seiler, Nucl. Eng. Des. **240**, 1975 (2010).
8. A. Löffler, K. Reuther, H. Engelhardt, D. Liu, M. Rettenmayr, Acta Mater. **91**, 34 (2015).
9. U. Bosenberg, M. Buchmann, M. Rettenmayr, J. Cryst. Growth **304**, 281 (2007).
10. S. Fischer, M. Zaloznik, J.M. Seiler, M. Rettenmayr, H. Combeau, J. Alloys Compd. **540**, 85 (2012).
11. H. Nguyen Thi, B. Drevet, J. Debierre, D. Camel, Y. Dabo, B. Billia, J. Cryst. Growth **253**, 539 (2003).
12. H. Nguyen Thi, G. Reinhart, A. Buffet, T. Schenk, N. Mangelinck-Noel, H. Jung, N. Bergeon, B. Billia, J. Härtwig, J. Baruchel, J. Cryst. Growth **310**, 2906 (2008).
13. A. Löffler, S. Lippmann, D. Liu, M. Rettenmayr, J. Cryst. Growth **408**, 49 (2014).
14. G. Salloum-Abou-Jaoude, G. Reinhart, H. Combeau, M. Založnik, T.A. Lafford, H. Nguyen-Thi, J. Cryst. Growth **411**, 88 (2015).
15. M. Buchmann, M. Rettenmayr, J. Cryst. Growth **284**, 544 (2005).
16. D.M. Liu, X.Z. Li, Y.Q. Su, P. Peng, L.S. Luo, J.J. Guo, H.Z. Fu, Acta Mater. **60**, 2679 (2012).
17. H. Engelhardt, D. Mey, S. Lippmann, D.M. Liu, S. Kiefer, M. Rettenmayr, J. Cryst. Growth **506**, 97 (2019).
18. Q. Zhang, H. Xue, Q. Tang, S. Pan, M. Rettenmayr, M. Zhu, Comput. Mater. Sci. **146**, 204 (2018).
19. S. Pan, Q. Zhang, M. Zhu, M. Rettenmayr, Acta Mater. **86**, 229 (2015).
20. H. Xing, M. Ji, X. Dong, Y. Wang, L. Zhang, S. Li, Mater. Des. **185**, 108250 (2020).
21. A.B. Phillion, M. Zaloznik, I. Spindler, N. Pinter, C.A. Aledo, G. Salloum-Abou-Jaoude, H.N. Thi, G. Reinhart, G. Boussinot, M. Apel, H. Combeau, Acta Mater. **141**, 206 (2017).
22. H. Xing, K. Ankit, X. Dong, H. Chen, K. Jin, Int. J. Heat Mass Transfer **117**, 1107 (2018).
23. D. Sun, H. Xing, X. Dong, Y. Han, Int. J. Heat Mass Transfer **133**, 1240 (2019).
24. H. Fang, Q. Tang, Q. Zhang, T. Gu, M. Zhu, Int. J. Heat Mass Transfer **133**, 371 (2019).
25. D. Sun, S. Pan, Q. Han, B. Sun, Int. J. Heat Mass Transfer **103**, 821 (2016).
26. J. Li, C. Guo, Y. Ma, Z. Wang, J. Wang, Acta Mater. **90**, 10 (2015).
27. H. Neumann-Heyme, K. Eckert, C. Beckermann, Acta Mater. **140**, 87 (2017).
28. G. Boussinot, M. Apel, Acta Mater. **122**, 310 (2017).
29. Q. Zhang, H. Fang, H. Xue, Q. Tang, S. Pan, M. Rettenmayr, M. Zhu, Scr. Mater. **151**, 28 (2018).
30. Q. Zhang, H. Fang, H. Xue, S. Pan, M. Rettenmayr, M. Zhu, Sci. Rep. **7**, 17809 (2017).